ACS ORGANIC & INORGANIC Au
AN OPEN ACCESS JOURNAL OF THE AMERICAN CHEMICAL SOCIETY

pubs.acs.org/orginorgau
Article

Purine-Functionalized Ferrocene Derivatives: Efficient Redox Catalysts for Oxidation of Methyl Blue and Reduction of Trinitrophenol

Sagar R. Sangani, Dax Patel, Ranjitsinh C. Dabhi, Tushar R. Sutariya, Sarfaraz Ahmed, and Rakesh Kumar Ameta*

Cite This: ACS Org. Inorg. Au 2025, 5, 47−61
Read Online
ACCESS | Metrics & More | Article Recommendations | Supporting Information

ABSTRACT: Herein, we report a novel organometallic series of potent purine-functionalized ferrocene derivatives (PFD) as redox catalysts. The synthesized PFDs were characterized through FTIR, $^{H/C}$NMR, and liquid chromatography−mass spectrometry (LCMS). Their thermogravimetric analysis (TGA) revealed the thermal stability up to 250 °C, and degradation was noted in the range of 300−500 °C. Their catalytic performance was tested and found for oxidative degradation of methyl blue (MB) up to 99% and reductive conversion of trinitrophenol (TNP) into triaminophenol (TAP) up to 92%, which is supported by their band gap analysis (2.7 eV). The highest unoccupied molecular orbital (HUMO) and lowest unoccupied molecular orbital (LUMO) calculations confirmed the stable geometry of PFDs, and negative values of HOMO and LUMO have supported the oxidation and reduction performance of PFDs as they were noted as Vb > Va > Vc > Vd > Ve due functions of variable substitution. The analysis of the Lagergren pseudo-first-order kinetic model, in support of catalytic performance, revealed that the mobility of dye/phenol molecules with the PFD is what regulates the catalytic conversion rate.

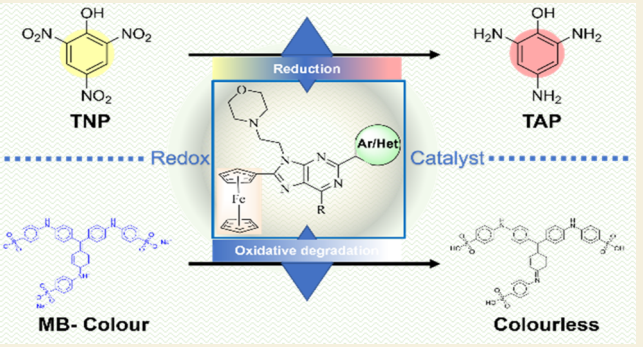

KEYWORDS: *DFT, ferrocene, purine, thermogravimetric analysis, degradation, photocatalytic activity*

1. INTRODUCTION

Increasingly, modern industries, particularly those in the textile, paper, and printing sectors, are generating more wastewater containing dyes and other organic phenolic pollutants. This escalation poses significant challenges for the treatment and decolorization processes of wastewater.[1,2] These pollutants are very harmful for humans as well as for climate change, causing environmental pollution. The inherent stability of dye and phenolic molecules against common degradation factors like light, heat, and oxidizing/reducing agents complicates the process.[3−6] Despite the utilization of various treatment methods, there remains a pressing need for new methods and efficient technologies that are both simple to operate and economically viable, especially those utilizing readily available resources.[7−12] Among the emerging technologies, photocatalysis stands out due to its capacity to utilize sustainable solar energy to facilitate reactions under mild conditions, making it a promising method for wastewater treatment.[13−16] Many of the metal-containing organometallic compounds have been utilized for the oxidation and reduction of such organic pollutants found in water.[17] In this regard, semiconductors used in Fenton-like processes can make hydroxyl radicals (•OH) when they react with ferrous salts and hydrogen peroxide. These radicals can remove both water-soluble and insoluble pollutants.[17,18] However, traditional Fenton reactions are inefficient, as only a small portion of hydrogen peroxide is converted into active oxidants for contaminant conversion.[19−21] This limitation necessitates the optimization of hydrogen peroxide utilization and the recycling of ferrous ions. Conventional Fenton processes also have problems, like needing a lot of chemical agents, only working at a narrow range of pH levels, being affected by complex agents like phosphate anions, and making a lot of sludge.[22,23] To address these challenges, researchers have investigated the use of organic transition metal compounds such as ferrocene (Fc) as heterogeneous Fenton catalysts, valued for their nontoxic, insoluble, and stable properties.[24−27] However, there

Received: July 29, 2024
Revised: September 25, 2024
Accepted: September 26, 2024
Published: November 18, 2024

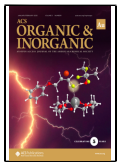

Scheme 1. Synthetic Steps Involved in the Synthesis of PFDs

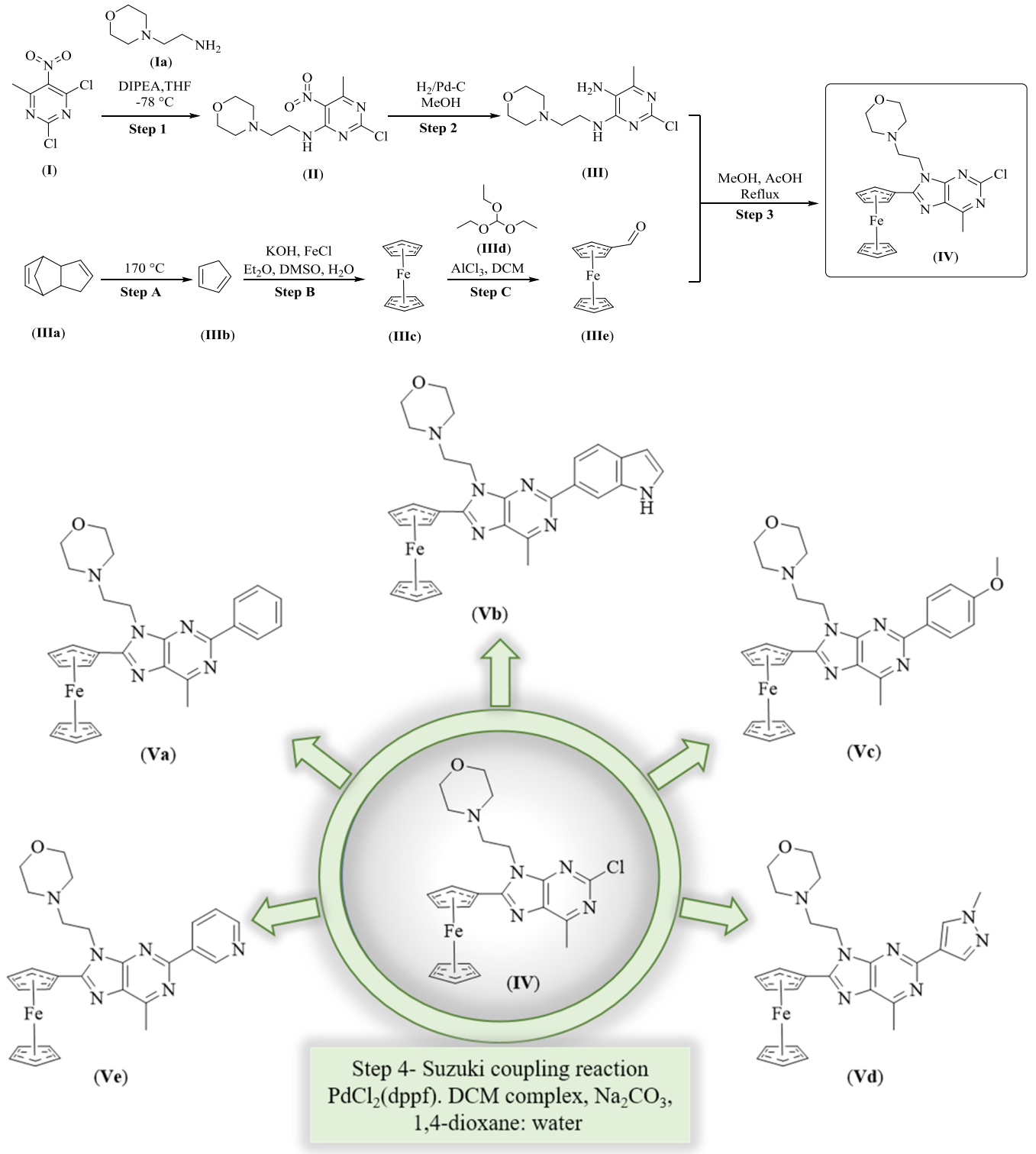

is a gap in understanding the application of these compounds in heterogeneous Fenton-like processes. Previous studies have primarily focused on immobilizing ferrocene on various substrates such as silica, mesoporous materials, carbon nanotubes, and MCM-48 for wastewater treatment.[16,28−31] Similarly, copper ions have potential as reactants with hydrogen peroxide in Fenton-like reactions, showing high rates of hydroxyl radical production across a broad pH range. However, research on using heterogeneous copper clusters as photocatalysts remains limited.[32−34] Thus, there is a need for new molecules for overcoming such issues for a productive environment. In this context, we report the synthesis of a novel series of purine-functionalized ferrocene derivatives (PFD) as reductive and oxidative catalysts for the degradation of trinitrophenol (TNP) and methyl blue (MB), respectively. Their catalytic performance has been supported with the band gap analysis, which is 2.7 eV, and suitable conduction and valence band positions for efficient sunlight-driven pollutant

https://doi.org/10.1021/acsorginorgau.4c00063
ACS Org. Inorg. Au 2025, 5, 47−61

degradation. Additionally, the highest unoccupied molecular orbitals (HOMO) and lowest unoccupied molecular orbital (LUMO) energy gaps calculated with density functional theory (DFT) revealed the suitability of PFDs as reductive and oxidative catalysts for degradation and conversion of MB and TNP, respectively. Our results show that the synthesized PFDs incorporating ferrocene achieve significantly faster and more effective oxidation of MB and reduction of TNP as compared to other studies. To our knowledge, these developed photocatalysts are good and most effective for degrading MB and reducing TNP under sunlight without the need for pH adjustments.

2. EXPERIMENTAL SECTION

All chemicals such as 2,4-dichloro-6-methyl-5-nitropyrimidine (I), 2-morpholinoethan-1-amine (Ia), and the $PdCl_2$(dppf)-DCM complex were acquired from Combi-Blocks and Sigma-Aldrich with 99.5% purity. Additional chemicals were also procured from Sigma-Aldrich and employed without further purification. For heating of the reactions, we used an oil bath as the heating source and a heating mantle (specially for step-A) for high temperature.

2.1. Synthetic Procedure of Intermediates and PFDs

The synthetic strategy for the PFDs is shown in Reaction Scheme 1, which also describes the various stages that went into synthesizing them.

2.1.1. Synthesis of 2-Chloro-6-methyl-*N*-(2-morpholinoethyl)-5-nitropyrimidin-4-amine (II). *N*-Ethyl-*N*,*N*-diisopropylamine (22.32 g, 173 mmol) and 2-morpholinoethan-1-amine (12.52 g, 96.15 mmol) in tetrahydrofuran (THF) (50 mL) were gradually mixed with a solution of 2,4-dichloro-6-methyl-5-nitropyrimidine (20 g, 96.15 mmol) in THF (500 mL) at −78 °C. TLC was used to track the reaction mixture's progress while it was being agitated for 30 min at −78 °C. After the combination was finished, it was dissolved in 1000 mL of ethyl acetate and then rinsed with a saturated $NaHCO_3$ solution and a brine solution. After being dried over sodium sulfate, the organic layer was filtered and concentrated under low pressure. After cleaning it up using column chromatography (silica gel, *n*-hexene/EtOAc = 7:3), we obtained IIa red solid (20 g, 68.93% yield). Anal. Calcd for $C_{11}H_{16}ClN_5O_3$: C, 43.79; H, 5.35; Cl, 11.75; N, 23.21; O, 15.91. Found: N, 23.10; O, 15.78; H, 5.12; C, 43.58; Cl, 11.65. Infrared (IR) (KBr, cm^{-1}): nmax/cm^{-1}: 570 (C−Cl), 1268 (C−O), 1200 (C−N), 1601 (C═C), 3330 (N−H), and 2812−2885 (C−H). ^{1}H NMR (400 MHz, DMSO-d_6). 2.51 (s, 3H), 2.94 (d, J = 4.8 Hz, 3H), 1.69 (m, 1H). Liquid chromatography−mass spectrometry (LCMS): 98%, MS (ESI) m/z: $[M + 1]^+$ Calcd for $C_{11}H_{16}ClN_5O_3$: 301.73; found 302.18.

2.1.2. Synthesis of 2-Chloro-6-methyl-*N*4-(2-morpholinoethyl)pyrimidine-4,5-diamine (III). To a solution of II (15 g, 49.71 mmol) in MeOH (300 mL) was added Pd/C (3 g, 60%). The reaction mixture was stirred at ambient temperature under a hydrogen gas atmosphere for 12 h. The progress of the reaction was monitored by TLC. After completion, the mixture was filtered through Celite, and the filtrate was concentrated to obtain III (9.8 g, 72.54% yield). Anal. Calcd for $C_{11}H_{18}ClN_5O$: C, 48.62; H, 6.68; Cl, 13.05; N, 25.77; and O, 5.89. Found: N, 25.59; O, 5.66; H, 6.47; C, 48.45; Cl, 12.95. IR (KBr, cm^{-1}): nmax/cm^{-1}: 3426−3219 (N−H), 2915−2810 (C−H), 1579 (C═C), 1303 (C−N aromatic), 1303 (C−N), and 549 (C−Cl). ^{1}H NMR (400 MHz, DMSO-d_6) δ 6.80 (m, 1H), 4.73 (s, 2H), 3.62 (m, 6H), 2.50 (m, 2H), 2.15 (m, 4H), 2.12 (m, 3H, J = 5.6 Hz). LCMS: 100%, MS (ESI) m/z: $[M + 1]^+$ Calcd for $C_{11}H_{18}ClN_5O$: 271.75; found 272.

2.2. Ferrocene Aldehyde and Scaffold Synthesis

2.2.1. Synthesis of Ferrocene (IIIc). A 50 mL portion of DME and 4.25 mL of newly distilled cyclopentadiene were combined in a 250 mL three-neck round-bottom flask with a nitrogen inlet and dropping funnel. The mixture was agitated in a nitrogen-filled environment. After that, 20 g of finely ground KOH was added, and the mixture was violently agitated for 15 min to generate a colorful mixture that included the cyclopentadienyl anion. In a different setting, 5 g of finely ground $FeCl_2{\cdot}4H_2O$ was dissolved in 20 mL of DMSO with nitrogen. Using a dropping funnel, this solution was gradually added to the first mixture, stirring continuously for 30 min. The resulting dark slurry is then added to a beaker with 80 g of crushed ice and 75 mL of 6 M hydrochloric acid after 30 min. All leftover KOH is dissolved and neutralized by giving the mixture a good shake. After the precipitate was filtered, it was rinsed with more water. A crude orange-colored ferrocene was gathered and vacuum-dried in the air. It was purified by sublimation to provide orange crystalline substance IIIc (5 g, 84% yield). Anal. Calcd for $C_{10}H_{10}Fe$: C, 64.56; H, 5.42; Fe, 30.02. Found: C, 64.45; H, 5.31; Fe, 29.74. IR (KBr, cm^{-1}): nmax/cm^{-1}: 1223 (C−H band), 1178 (C−H band), 1095, 1053 (C−H band). ^{1}H NMR (400 MHz, chloroform-d) δ 4.23 (s, 10H). LCMS: 96.46%, MS (ESI) m/z: $[M + 1]^+$ Calcd for $C_{10}H_{10}Fe$: 186.01; found 186.

2.2.2. Synthesis of Ferrocene Carboxaldehyde (IIIe). Dichloromethane (75 mL) and charged dry ferrocene (5 g, 26.88 mmol) were placed in a three-neck flask. Next, dropwise addition of triethyl orthoformate (19.6 g, 132.17 mmol) was made to the mixture while it was continuously stirred. Anhydrous $AlCl_3$ (30 g) was gradually added once the ferrocene had completely dissolved, and the reaction mixture was agitated for 3 h at room temperature. After the reaction was finished, the reaction mixture was extracted using 100 mL of diethyl ether and quenched with a saturated solution of sodium hydrosulfite. First, low pressure was used to concentrate the organic extract. Red solid IIIe (3.5 g, yield: 70%) was obtained by chromatography on silica gel (petroleum ether: ethyl acetate = 5:1) after the remaining material had been cleaned up. Anal. Calcd for $C_{11}H_{10}FeO$: C, 61.73; H, 4.71; Fe, 26.09; O, 7.47. Found: C, 60.65; H, 4.11; Fe, 25.89; O, 7.12. IR (KBr, cm^{-1}): nmax/cm^{-1}: 2830 (C−H stretch), 1660 (C═O), ^{1}H NMR (400 MHz, Chloroform-d) δ 9.99 (s, 1H), 4.82 (s, 2H), 4.64 (s, 2H), 4.30 (s, 5H). LCMS: 93.61%, MS (ESI) m/z: $[M + 1]^+$ Calcd for $C_{11}H_{10}FeO$: 214.01; found 215.07.

2.2.3. Synthesis of Ferrocenyl Scaffold (IV). 50 mL of methanol was added to solution III (5 g, 18.40 mmol) and solution IIIa (5.91 g, 27.60 mmol), followed by the addition of 50 mL of acetic acid. For 12 h, the mixture was heated to 100 °C while being stirred. The reaction's evolution was monitored by TLC. Following the completion of the reaction, the reaction mixture was added to a saturated $NaHCO_3$ solution, and the product was extracted using dichloromethane. After the combined organic layer was cleaned with brine solution, dried over sodium sulfate, and concentrated under low pressure, crude material was extracted. After that, it was further purified using *n*-hexane/ethyl acetate (1:1) silica gel column chromatography to give IV (5 g, yield: 58.34%). Anal. Calcd for $C_{22}H_{24}ClFeN_5O$: C, 56.73; H, 5.19; Cl, 7.61; Fe, 11.99; N, 15.04; and O, 3.44. Found: C, 56.73; H, 5.19; Cl, 7.61; Fe, 11.99; N, 15.04; and O, 3.44. IR (KBr, cm^{-1}): nmax/cm^{-1}: 2997 (C−H, aromatic), 1569−1436 (C═C), 1310 (C−N), 1105 (m, C−H), 1006 (w, C−H), 571 (C−Cl),456 (st, 456). ^{1}H NMR (400 MHz, DMSO-d_6) δ 5.05 (d, J = 10.5 Hz, 2H), 4.55−4.69 (m, 4H), 4.27 (dd, J = 10.4, 3.5 Hz, 4H), 3.51 (m, 4H), 2.73−2.82 (m, 4H), 2.69 (dd, J = 10.3, 3.6 Hz, 2H), 2.63 (s, 3H). ^{13}C{^{1}H} NMR (101 MHz, DMSO-d_6) δ 158.3, 156.4, 154.8, 151.4, 132.0, 72.4, 71.4, 70.3, 69.7, 68.6, 66.6, 57.4, 53.9, 41.6, 40.6, 39.8, 19.5. LCMS: 96%, MS (ESI) m/z: $[M + 1]^+$ Calcd for $C_{22}H_{24}ClFeN_5O$: 465.76; found 466.23.

2.3. Synthesis of PFDs (Va−Ve)

2.3.1. *Synthesis of Va* (Cyclopenta-1,3-dien-1-yl(2-(6-methyl-9-(2-morpholinoethyl)-2-phenyl-9*H*-purin-8-yl)cyclopenta-1,4-dien-1-yl)iron). A 200 mg portion (0.43 mol) of solution IV was mixed with 1,4-dioxane and 68 mg (0.55 mol) of phenylboronic acid. After that, a 2 mL aqueous solution of Na_2CO_3 was added, and argon was used to let the mixture degas for 10 min. After the gas was left to stand for a further five min, 34 mg of the 1,1-bis(diphenylphosphino)-ferrocene/dichloropalladium-dichloromethane complex (0.042 mmol) was applied. After that, the mixture was heated to 110 °C for an hour. After the reaction was finished, dichloromethane was

https://doi.org/10.1021/acsorginorgau.4c00063
ACS Org. Inorg. Au 2025, 5, 47−61

used to extract the reaction mixture, which was then diluted with water. To produce a crude material, the blended organic extracts were subjected to a variety of processes, such as washing in brine solution, drying with sodium sulfate, and concentration under decreased pressure. After that, this substance was purified using *n*-hexane/ethyl acetate (2:3) silica gel column chromatography to yield Va. (100 mg, 45.90%). Anal. Calcd for $C_{28}H_{29}FeN_5O$: C, 66.28; H, 5.76; Fe, 11.01; N, 13.80; and O, 3.15. Found: C, 66.15; H, 5.65; Fe, 10.85; N, 13.67; and O, 3.02. IR (KBr, cm^{-1}): nmax/cm^{-1}: 3564 (N−H), 2961 (C−H, aromatic), 1541−1504 (C═C), 1366 (C−N), 1108 (m, C−H), 1067 (w, C−H). ^{1}H NMR (400 MHz, DMSO-d_6) δ 8.48 (d, J= 7.5 Hz, 2H), 7.53 (dt, J = 12.3, 6.9 Hz, 3H), 5.09 (s, 2H), 4.73 (t, J = 6.6 Hz, 2H), 4.66 (s, 2H), 4.28 (s, 4H), 3.49 (t, J = 4.6 Hz, 4H), 2.87 (t, J = 6.5 Hz, 2H), 2.79 (s, 3H), 2.56 (d, J = 4.8 Hz, 4H). ^{13}C{^{1}H} NMR (101 MHz, DMSO-d_6) δ: 156.5, 155.9, 155.4, 153.9, 138.5, 134.6, 131.7, 130.3, 129.0, 127.9, 73.2, 71.2, 70.2, 69.6, 66.6, 57.8, 53.9, 41.0, 20.0. LCMS: 99%, MS (ESI) m/z: $[M + 1]^+$ Calcd for $C_{28}H_{29}FeN_5O$: 507.17; found 509.14.

2.3.2. *Synthesis of Vb* (Cyclopenta-1,3-dien-1-yl(2-(2-(indolin-6-yl)-6-methyl-9-(2-morpholinoethyl)-9*H*-purin-8-yl)-cyclopenta-1,4-dien-1-yl)iron). A solution of IV (200 mg, 0.43 mmol) and 1*H*-indol-6-yl-boronic acid (68 mg, 0.55 mmol) in 1,4-dioxane, 2 M aqueous solution of Na_2CO_3 (1 mL) was added, and argon was allowed to degas for 10 min. 34 mg of the 1,1-bis(diphenylphosphino)ferrocene/dichloropalladium-dichloromethane complex was introduced after 5 min of degassing of the reaction mixture and then heated to 110 °C for an hour. After the reaction was finished, dichloromethane was used to extract the reaction mixture, which was then diluted with water. Blended organic extracts were dried over sodium sulfate, washed with brine solution, and then concentrated under low pressure to yield crude material. After that, silica gel column chromatography (*n*-hexane/ethyl acetate = 1:1) was used to refine it and obtain Vb (120 mg, yield: 51.14%). Anal. Calcd for $C_{30}H_{30}FeN_6O$: C, 65.94; H, 5.53; Fe, 10.22; N, 15.38; O, 2.93. Found: C, 65.78; H, 5.35; Fe, 10.10; N, 15.25; O, 2.76. IR (KBr, cm^{-1}): nmax/cm^{-1}: 3528 (N−H), 2920−2852 (C−H, aromatic), 1577−1525 (C═C), 1308 (C−N), 1105 (m, C−H), 1005 (w, C−H). ^{1}H NMR (400 MHz, DMSO-d_6) δ 11.25 (s, 1H), 8.73 (s, 1H), 8.30 (d, J = 8.7 Hz, 1H), 7.49 (d, J = 8.6 Hz, 1H), 7.40 (t, J = 2.7 Hz, 2H), 6.59 (s, 1H), 5.06 (t, J = 2.0 Hz, 2H), 4.72 (t, J = 6.5 Hz, 2H), 4.60−4.66 (m, 2H), 4.27 (s, 4H), 3.50 (t, J = 4.5 Hz, 4H), 2.87 (t, J = 6.5 Hz, 2H), 2.77 (s, 3H), 2.57 (m, 4H). ^{13}C{^{1}H} NMR: (101 MHz, DMSO-d_6) δ: 158.3, 155.7, 154.4, 153.9, 137.5, 130.9, 129.6, 128.3, 126.7, 121.7, 120.6, 111.6, 102.7, 73.5, 70.9, 70.1, 69.4, 66.6, 57.8, 55.4, 53.9, 40.9, 25.4, 20.0. LCMS: 100%, MS (ESI) m/z: $[M + 1]^+$ Calcd for $C_{30}H_{30}FeN_6O$: 546.18; found 547.31.

2.3.3. *Synthesis of Vc* (Cyclopenta-1,3-dien-1-yl(2-(2-(4-methoxyphenyl)-6-methyl-9-(2-morpholinoethyl)-9*H*-purin-8-yl)cyclopenta-1,4-dien-1-yl)iron). Following the addition of 2 M aqueous solution of Na_2CO_3 (1 mL) and the degassing of the mixture with argon for 10 min, 85 mg of 4-methoxyphenylboronic acid (0.55 mmol) in 1,4-dioxane was mixed with a IV solution (200 mg, 0.43 mmol). Degassing for a further 5 min was followed by the addition of 34 mg (0.042 mmol) of 1,1-bis(diphenylphosphino)ferrocene/dichloropalladium-dichloromethane complex. After that, the mixture was heated to 110 °C for an hour. After the reaction was finished, dichloromethane was used to extract the reaction mixture, which was then diluted with water. Blended organic extracts were dried over sodium sulfate, washed with brine solution, and then concentrated under low pressure to yield crude material, which was further purified using silica gel column chromatography (*n*-hexane/ethyl acetate = 2:3), and the pure product obtained was Vc (110 mg, yield: 47.66%). Anal. Calcd for $C_{29}H_{31}FeN_5O_2$: C, 64.81; H, 5.81; Fe, 10.39; N, 13.03; and O, 5.95. Found: C, 64.75; H, 5.74; Fe, 10.27; N, 12.85; O, 5.78 IR (KBr, cm^{-1}): nmax/cm^{-1}: 3594 (N−H), 2950 (C−H, aromatic), 1573−1521 (C═C), 1354 (C−N), 1105 (m, C−H), 1064 (w, C−H). ^{1}H NMR (400 MHz, DMSO-d_6) δ 8.41 (d, J = 8.5 Hz, 2H), 7.08 (d, J = 8.4 Hz, 2H), 5.06 (s, 2H), 4.61−4.74 (m, 4H), 4.27 (s, 4H), 3.85 (s, 3H), 3.49 (t, J = 4.6 Hz, 4H), 2.85 (t, J = 6.6 Hz, 2H), 2.75 (s, 3H), 2.52−2.58 (m, 4H). ^{13}C{^{1}H} NMR (101 MHz, DMSO-d_6) δ: 161.2, 156.6, 155.9, 154.8, 153.8, 131.1, 129.5, 114.3, 73.2, 71.1, 70.2, 69.5, 66.6, 57.7, 55.7, 53.9, 40.9, 39.3, 19.9. LCMS: 95%, MS (ESI) m/z: $[M + 1]^+$ Calcd for $C_{29}H_{31}FeN_5O_2$: 537.18; found 538.32.

2.3.4. *Synthesis of Vd* (Cyclopenta-1,3-dien-1-yl(2-(6-methyl-2-(1-methyl-1*H*-pyrazol-4-yl)-9-(2-morpholinoethyl)-9*H*-purin-8-yl)cyclopenta-1,4-dien-1-yl)iron). In 1,4-dioxane, a mixed solution containing IV (200 mg, 0.43 mmol) and 1-methyl pyrazole-4-boronic acid pinacol ester (116 mg, 0.55 mmol) was mixed with a 1 mL solution of 2 M aqueous Na_2CO_3. After that, argon was used to degas the mixture for 10 min. 34 mg of the 1,1-bis(diphenylphosphino)ferrocene/dichloropalladium-dichloromethane complex (0.042 mol) was added after the mixture had been degassed for an additional 5 min. After that, the mixture was heated to 110 °C for an hour. After the reaction was finished, dichloromethane was used to extract the reaction mixture, which was then diluted with water. Blended organic extracts were dried over sodium sulfate, washed with brine solution, and then concentrated under low pressure to yield crude material, which was further purified by silica gel column chromatography (*n*-hexane: ethyl acetate = 2:3) to obtain Vd (100 mg, yield: 45.54%). Anal. Calcd for $C_{26}H_{29}FeN_7O$: C, 61.06; H, 5.72; Fe, 10.92; N, 19.17; and O, 3.13. Found: C, 60.92; H, 5.64; Fe, 10.78; N, 19.02; O, 3.05. IR (KBr, cm^{-1}): nmax/cm^{-1}: 3500 (N−H), 2920−2843 (C−H, aromatic), 1565−1531 (C═C), 1313 (C−N), 1104 (m, C−H), 1002 (w, C−H). ^{1}H NMR (400 MHz, DMSO-d_6) δ 8.32 (s, 1H), 8.01 (s, 1H), 5.04 (s, 2H), 4.65 (d, J = 6.3 Hz, 2H), 4.63 (s, 2H), 4.27 (s, 4H), 3.93 (s, 3H),3.49 (t, J = 4.5 Hz, 4H),2.82 (t, J = 6.5 Hz, 2H), 2.70 (s, 3H), 2.51(m, 2H). ^{13}C{^{1}H} NMR (101 MHz, DMSO-d_6) δ: 156.0, 154.2, 153.6, 138.8, 131.5, 130.6, 123.6, 73.4, 70.9, 70.1, 69.4, 66.6, 57.8, 53.9, 40.8, 39.9, 19.8. LCMS: 93%, MS (ESI) m/z: $[M + 1]^+$ Calcd for $C_{26}H_{29}FeN_7O$: 511.18; found 512.29.

2.3.5. *Synthesis of Ve* (Cyclopenta-1,3-dien-1-yl(2-(6-methyl-9-(2-morpholinoethyl)-2-(pyridin-3-yl)-9*H*-purin-8-yl)-cyclopenta-1,4-dien-1-yl)iron). A 200 mg portion of IV (0.43 mmol) and 69 mg of pyridine-3-yl-boronic acid (0.55 mmol) in 1,4-dioxane were combined with a 2 M aqueous solution of Na_2CO_3 (1 mL). After that, argon was used to degas the mixture for 10 min. After a further 5 min of degassing, 34 mg of the 1,1-bis-(diphenylphosphino)ferrocene/dichloropalladium-dichloromethane complex (0.042 mmol) was added. After that, the mixture was heated to 110 °C for an hour. After the reaction was finished, dichloromethane was used to extract the reaction mixture, which was then diluted with water. Blended organic extracts were dried over sodium sulfate, washed with brine solution, and then concentrated under low pressure to yield crude material, which was further purified by silica gel column chromatography (*n*-hexane: ethyl acetate = 2:3) to obtain Ve (99 mg, yield: 45.35%). Anal. Calcd for $C_{27}H_{28}FeN_6O$: C, 63.79; H, 5.55; Fe, 10.98; N, 16.53; and O, 3.15. Found: C, 63.68; H, 5.35; Fe, 10.78; N, 16.32; O, 2.87. IR (KBr, cm-1): nmax/cm^{-1}: 3581 (N−H), 2957 (C−H, aromatic), 1574−1524 (C═C), 1319 (C−N), 1106 (m, C−H), 1010 (w, C−H). ^{1}H NMR (400 MHz, DMSO-d_6) δ 9.61 (s, 1H), 8.67−8.77 (m, 2H), 7.57 (d, J = 7.3 Hz, 1H), 5.10 (s, 2H), 4.73 (t, J = 6.5 Hz, 2H), 4.67 (s, 2H), 4.28 (s, 4H),3.48 (t, J = 4.6 Hz, 4H), 2.83 (d, J = 25.7 Hz, 2H), 2.80 (s, 3H), 2.56 (m, 4H). ^{13}C{^{1}H} NMR (101 MHz, DMSO-d_6) δ: 160.4, 156.2, 155.9, 153.8, 150.2, 149.2, 147.4, 139.8, 135.1, 132.0, 109.2, 92.5, 87.9, 79.9, 71.3, 70.2, 69.6, 66.6, 64.2, 57.7, 53.9, 49.1, 40.6, 39.4, 30.6, 19.9. LCMS: 94%, MS (ESI) m/z: $[M + 1]^+$ Calcd for $C_{27}H_{28}FeN_6O$: 508.18; found 509.28.

2.4. Characterization

The structures of the compounds were clarified using FTIR (Bruker) spectroscopy with an ATR sensor within the range from 4000 to 400 cm^{-1}. A Bruker-Biospin Avance-III 400 MHz FT-NMR spectrometer was used to produce 1H- and 13C-NMR spectra in DMSO-d_6 (NMR, 99.99%). The internal standard for chemical shifts was a TMS. Mass spectra were obtained using an Agilent Q-TOF LC/MS system operating in ESI+ mode and a mobile phase consisting of acetonitrile and water in a 3:7 ratio. Elements of analysis were carried out using the Euro Vector tool. The thermal stability of the synthesized compounds was assessed using thermogravimetric analysis (TGA)

https://doi.org/10.1021/acsorginorgau.4c00063
ACS Org. Inorg. Au 2025, 5, 47−61

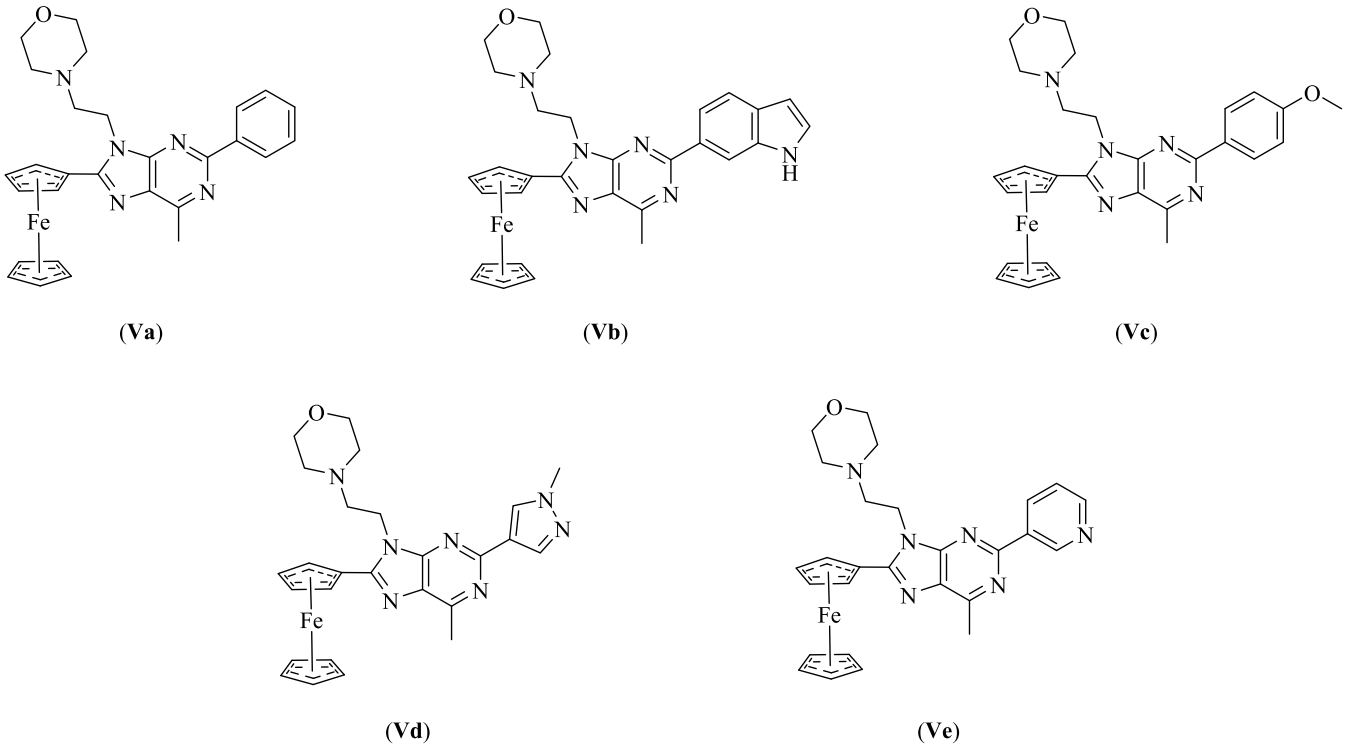

Figure 1. Structures of the synthesized PFDs.

[5000/2960 TA Instruments]. The measurement was performed in an N_2 atmosphere, heating from 30 to 500 °C at a rate of 5 °C min^{-1}.

2.5. General Procedure for Catalytical Activity

2.5.1. Oxidative Dye Degradation. An MB concentration of 50 mg/L was dissolved in water to create a dye model. 100 μL of fresh H_2O_2 and 10 mg of photocatalyst were added to this solution. After that, the mixture was exposed to the sun, and every five min, 3 mL of the sample was taken for UV−visible examination. The photocatalyst was centrifuged, cleaned with water, and dried at 80 °C for reusability tests following the mixture's complete discoloration. All of the experiments were carried out in the presence of sunlight, with 25 mW/m^2 intensity.

2.5.2. Reduction of Trinitrophenol. In a 10 mL beaker, a typical catalytic test reaction was carried out. Two milliliters of a 10^{-1} M sodium borohydride (SBH) solution was mixed with six milliliters of an aqueous solution containing ten times as much TNP (10^{-4} M). Ten milligrams of the complex was then added to this mixture. The UV/Visible spectra were taken after 30 min, where a decrease in absorbance was observed. Deionized water was used as a reference for background correction where deionized water was taken in reference as well as sample cells of the instrument. All of the experiments were carried out in the presence of sunlight with 25 mW/m^2 intensity.

2.6. DFT Analysis

We performed quantum chemistry computations in a vacuum using the B3LYP/6-31G (d, p) basis set and the DFT approach. The Gaussian O9W computer package and Gauss-View molecular visualization tool were used for all calculations.

3. RESULTS AND DISCUSSION

3.1. Characterizations and Structural Illustration

A series of organometallic compounds, PFD (Va−Ve), was synthesized, and their structures are shown in Figure 1.

The characterization of PFD, along with II, III, ferrocene (IIIc), ferrocene carboxaldehyde (IIIe), and ferrocenyl scaffold (IV), depicted in Scheme 1, was effectively conducted using various analytical methods. Compound II demonstrated distinctive infrared (IR) peaks at 3330 nm (NH), 1493 nm (NO2), and 570 cm^{-1} (C−Cl), indicating specific functional groups. Its 1H nuclear magnetic resonance (NMR) spectrum in DMSO-d_6 solvent revealed resonances at δ 8.69 (multiplet, 1H), 2.94 (doublet, J = 4.8 Hz, 3H), and 2.51 (singlet, 3H), confirming its chemical structure. Liquid chromatography−mass spectrometry (LCMS) analysis displayed a major peak at m/z 302.18 $(M + 1)^+$, with an exact mass of 301.73, affirming the molecular weight and composition of Compound II. Compound III exhibited IR peaks at 3426−3219 (NH), 2915−2810 (C−H), and 1579 cm^{-1} (C═C), confirming the presence of specific functional groups. Its ^{1}H NMR spectrum in the DMSO-d_6 solvent confirmed the chemical structure, with resonances at δ 4.73 for the amine group. LCMS analysis provided a major peak at m/z 272 $(M + 1)^+$, with an exact mass of 271.75, verifying the molecular weight and composition of Compound III. Ferrocene (IIIc) was confirmed by IR spectroscopy, showing characteristic peaks at 1223 and 1178 cm^{-1} corresponding to CH bending vibrations in the cyclopentadienyl rings. The ^{1}H NMR spectrum displayed a single peak at δ 4.23 (s, 10H), confirming the expected chemical environment of cyclopentadienyl protons. LCMS analysis yielded a molecular ion peak at m/z 186 $[M + H]^+$, aligning with the calculated mass of 186.01, validating the identity of ferrocene. Ferrocene carboxaldehyde (IIIe) exhibited characteristic peaks at 2830 (C−H stretch) and 1660 cm^{-1} (C═O). The ^{1}H NMR spectrum revealed peaks at δ 9.99 for the aldehyde proton, consistent with the anticipated structure. LCMS analysis unveiled a molecular ion peak at m/z 215.07 $[M + H]^+$, along with an exact mass of 214.01, further confirming the compound's identity and purity. Ferrocenyl Scaffold (IV) displayed IR characteristic peaks for C═C (1569−1436 cm^{-1}), C−N (1310 cm^{-1}), and C−Cl (571 cm^{-1}) bonds. Notably, the absence of a free NH proton in the 1H NMR spectrum confirmed novel cyclization in ferrocenyl

https://doi.org/10.1021/acsorginorgau.4c00063
ACS Org. Inorg. Au 2025, 5, 47−61

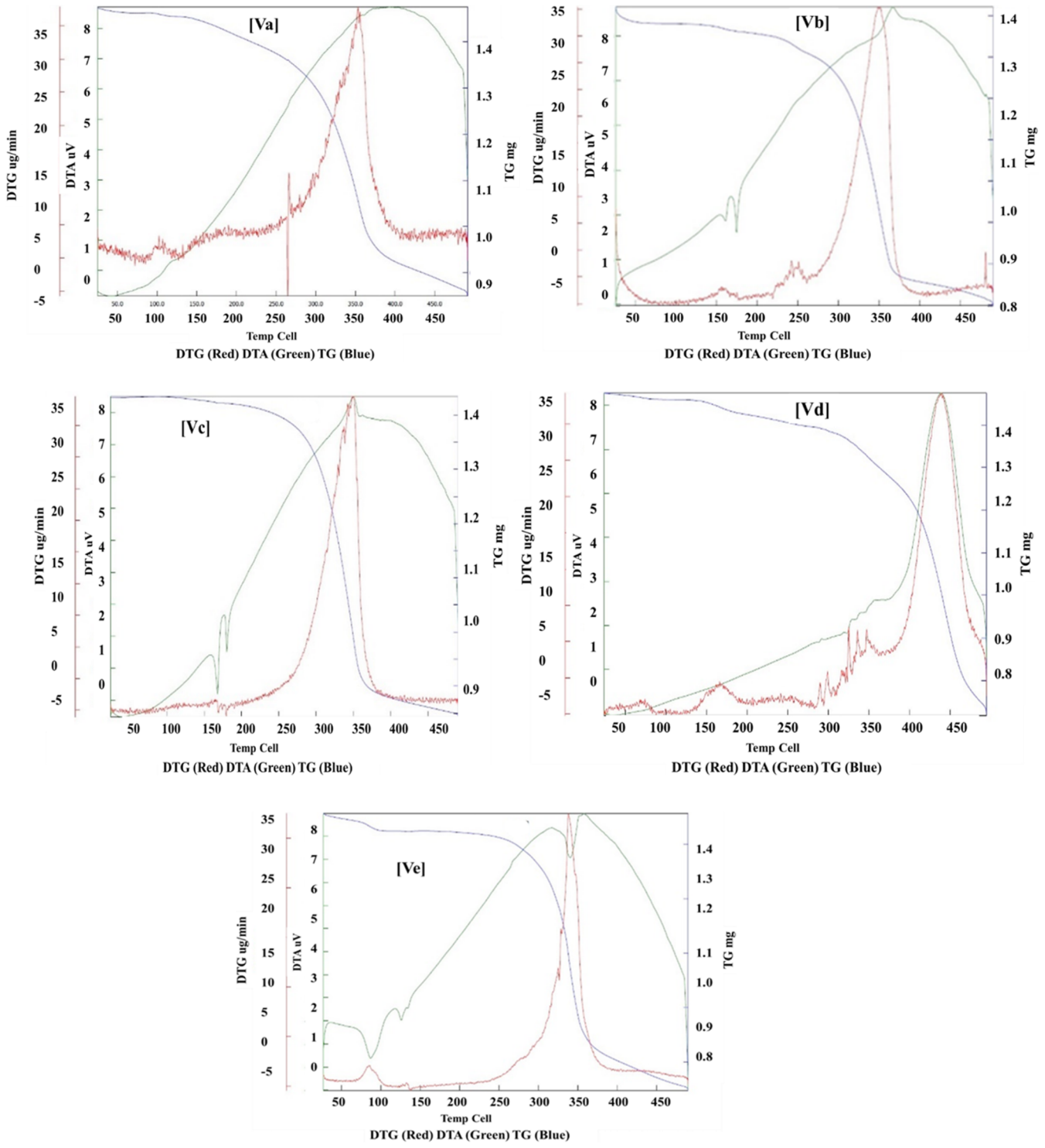

Figure 2. TGA curves are for PFDs.

scaffold (IV). LCMS indicated a prominent peak at 466.23 (M + 1)$^+$, with the exact mass calculated at 465.76, providing additional affirmation of the successful synthesis and meticulous characterization of ferrocenyl scaffold (IV).

For PFD compound Va, the IR spectrum displayed characteristic peaks at 2961 (C−H, aromatic) and 1541−1504 cm^{-1} (C═C stretching). The ^{1}H NMR spectrum exhibited distinctive signals, including δ 7.53 and 8.48 aromatic rings. LCMS analysis showed a molecular ion peak at m/z 509.14 [M + H]$^+$. Vb revealed distinctive peaks at 3528 cm^{-1} (N−H), corroborating the functional groups in the molecule. ^{1}H NMR spectroscopy provided insight into indole aromatic, and the N−H proton confirms the structure. Furthermore, LCMS unequivocally confirmed Vb's molecular weight with the [M + H]$^+$ ion at m/z 547.31, providing definitive evidence of its molecular identity. Vc displayed characteristic IR peaks at 2950 cm^{-1}, confirming the presence of methoxy functional groups. ^{1}H NMR reveals signals at δ 2.75 methoxy CH_3, contributing to its structural elucidation. LCMS analysis indicated the molecular ion peak at m/z 538.32 [M + H]$^+$,

https://doi.org/10.1021/acsorginorgau.4c00063
ACS Org. Inorg. Au 2025, 5, 47−61

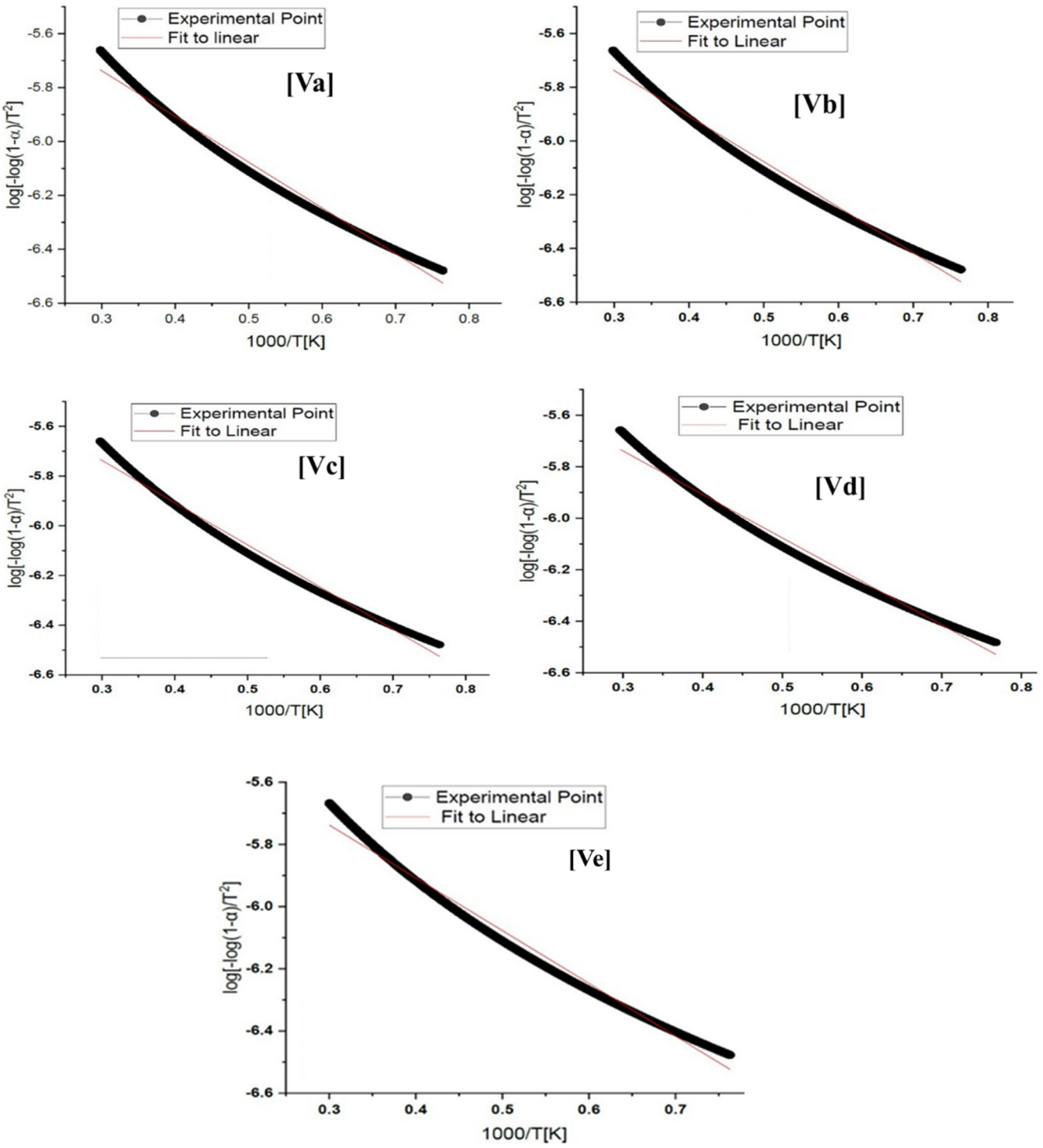

Figure 3. Activation energy analysis using the TGA curve.

Table 1. Activation Energy of PFDs Was Calculated from TGA Analysis

PFD	slop value $-E/2.303RT$	activation energy
Va	−1.68699	E_a = −14.02 kJ/mol
Vb	−1.69690	E_a = −14.12 kJ/mol
Vc	−1.69833	E_a = −14.14 kJ/mol
Vd	−1.68943	E_a = −14.03 kJ/mol
Ve	−1.69682	E_a = −14.11 kJ/mol

closely matching the calculated exact mass of 537.18, thereby validating the compound's molecular weight. Vd showed distinct peaks at δ 2.70, confirming the presence of pyrazole methyl groups. LCMS revealed a major peak at m/z 512.29 $[M + H]^+$, validating the compound's molecular weight. Ve showed characteristic IR peaks at 1319 cm^{-1} (C−N), indicating a pyridine C−N bond. LCMS confirmed the mass (m/z = 509.28 $[M + H]^+$) of compound Ve.

https://doi.org/10.1021/acsorginorgau.4c00063
ACS Org. Inorg. Au 2025, 5, 47−61

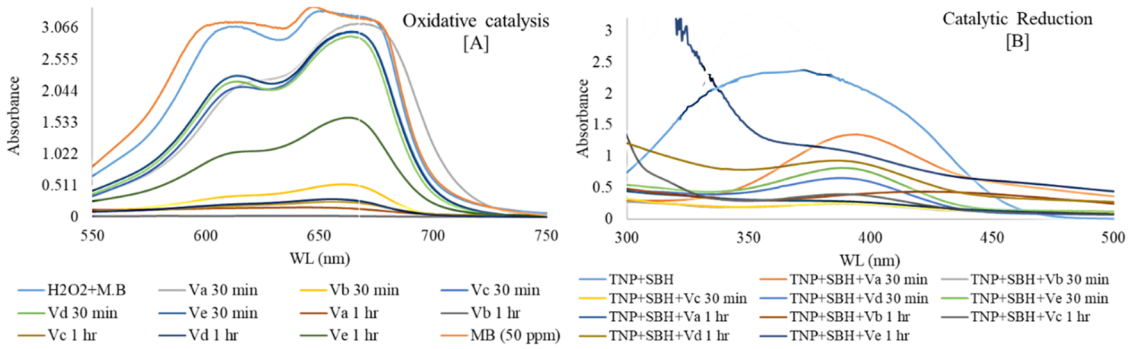

Figure 4. PFDs as photocatalyst for (A) methyl blue degradation and (B) catalytical reduction of trinitrophenol.

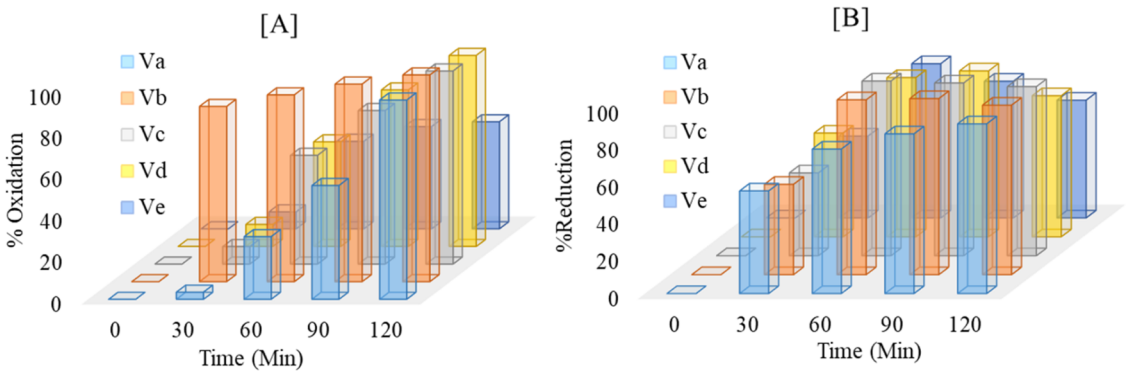

Figure 5. Oxidation and reduction performance of PFDs as photocatalysts; (A) % oxidation of MB, and (B) % reduction of TNP.

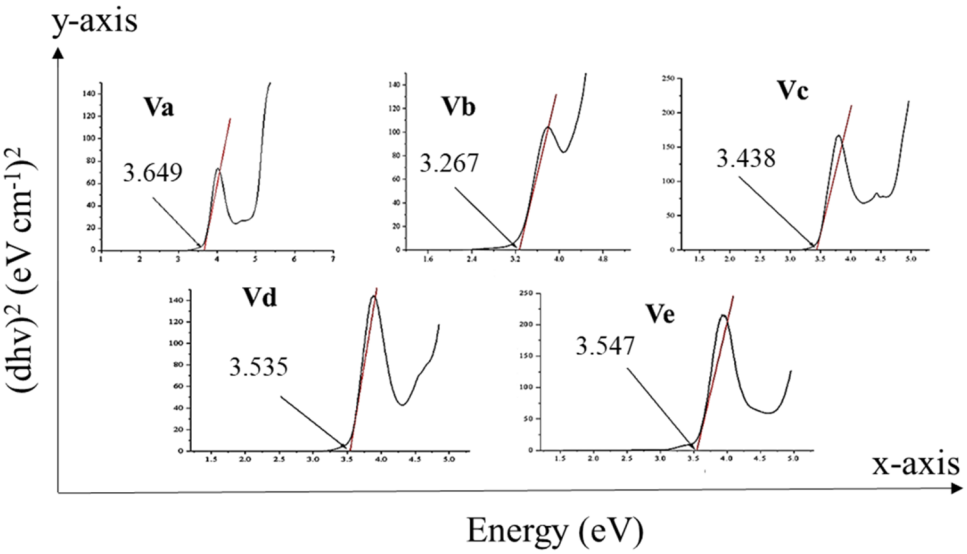

Figure 6. Band gap analysis of PFDs by UV/visible examination.

3.2. TGA Analysis

The TGA curves of all PFD showed a small thermal transition near around 100 °C, which is attributed to moisture (Figure 2). The second thermal resilience is near around 260 °C for all PFD, which may be due to either the removal of residual carbon postcombustion or attributed to the decomposition of the complex.

Kinetic and thermodynamic parameters for a step 1 decomposition are computed using the Coats−Redfern method for a single heating rate.[35−40] The following formulas, which have been published in the literature, are used to calculate activation energy.[41] The approach involves estimating α (degree of response) and $g(\alpha)$ (integral function of conversion) using several factors, which are elaborated upon thereafter. The function $g(\alpha)$ is given by

$$g(\alpha) = \frac{ART^2}{\beta E}\left[1 - \frac{2RT}{E}\right]e^{-E/RT}$$

which can be rearranged to give

$$-\ln\frac{g(\alpha)}{T^2} = -\ln\frac{AR}{\beta E}\left[1 - \frac{2RT}{\beta E}\right] + \frac{E}{RT}$$

https://doi.org/10.1021/acsorginorgau.4c00063
ACS Org. Inorg. Au 2025, 5, 47−61

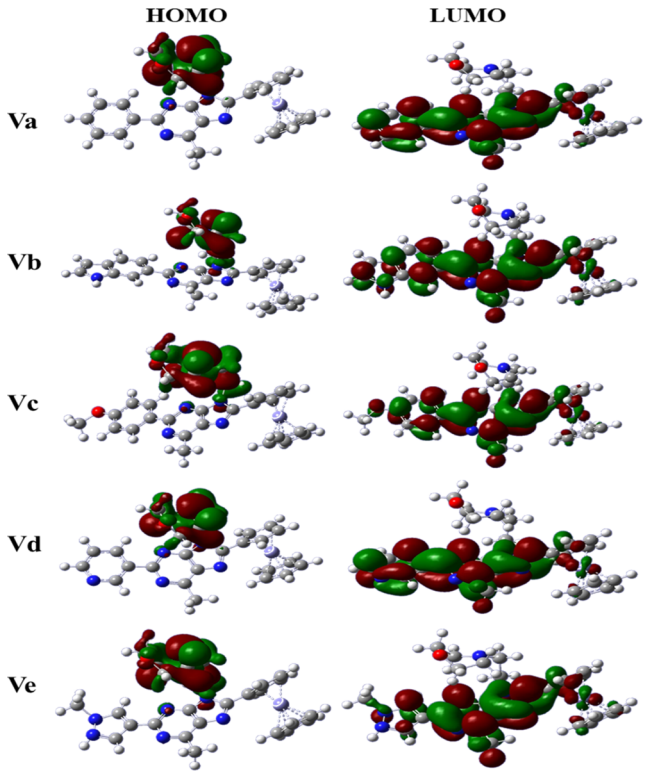

Figure 7. Graphical demonstration of HOMO LUMO of PFDs.

Table 2. HOMO LUMO Energy and Energy Gap for PFDs

sr. no.	compound no.	HOMO energy	LUMO energy	energy gap (eV)
1	Va	−0.18309	−0.04946	0.13363
2	Vb	−0.18246	−0.04272	0.13974
3	Vc	−0.18182	−0.04885	0.13332
4	Vd	−0.18526	−0.05467	0.13059
5	Ve	−0.1884	−0.06206	0.12634

The TG curve is used to determine a fractional mass loss (α) and the corresponding $(1-\alpha)^n$, where n is dependent on the reaction model.

$$-\log\frac{1-(1-\alpha)^{1-n}}{T^2(1-n)} = \log\frac{AR}{\beta E}\left[1-\frac{2RT}{E}\right]-\frac{E}{2.303RT},\quad n\neq 1$$

$$-\log\frac{-\log(1-\alpha)}{T^2} = \log\frac{AR}{\beta E}\left[1-\frac{2RT}{E}\right]-\frac{E}{2.303RT},\quad n=1$$

This calculation indicates that the activation energy (Figure 3), tabulated in Table 1 for the thermal decomposition reactions of PFDs, is almost the same for all PFDs.

3.3. Catalytical Evaluation

PFDs have shown catalytic activity in both oxidation and reduction when tested against MB and TNP, respectively. One of the most crucial variables influencing dye adsorption and degradation is the solution pH, which has a direct impact on photocatalyst redox reversibility. Without any modifications, the PFDs combination comprising MB and photocatalyst had a pH of 5.5.

In the case of MB degradation, the solution of H_2O_2 and MB showed an absorption maximum at 670 nm, which was found to be stable for several days, indicating no oxidation of MB due to H_2O_2. After mixing the PFDs, the absorbance decreased, as shown in Figure 4A, which is due to the start of MB oxidation in the presence of PFD. The % oxidation of MB concerning time is shown in Figure 5A, calculated as below, where PFD Vb has shown 99% oxidation of MB after 120 min.

$$\%\ \text{oxidation/reduction} = \frac{C_{\text{dye},0}-C_{\text{dye}}}{C_{\text{dye},0}}\times 100\%$$

where $C_{\text{dye},0}$ is the initial dye concentration and C_{dye} is the dye concentration after adsorption.

The dependence of oxidation due to the presence of functional groups in PFDs, for instance, PFDs Va−Ve have shown 96, 99.60, 93.01, 92.03, and 51.55% oxidative degradation of MB due to the presence of benzene, 1*H*-indol, anisole, pyridine, and 1-methyl-1*H*-pyrazole associated with the core ferrocene scaffold, respectively. Similarly, in the case of the reduction of TNP, the mixed solution of SBH and TNP has shown an absorbance near around 400 nm due to the formation of a phenolate ion, which was found to be stable for many days, inferring no reduction of TNP due to the presence of SBH (Figure 4B). After the PFD solution was mixed, the absorbance was found to be decreased due to the reduction of TNP into aminophenol. Similar to oxidation, Vb has shown higher reduction activity as compared to others, such as $Vb_{91.24}$ > $Va_{91.12}$ > $Vc_{90.94}$ > $Vd_{75.89}$ > $Ve_{63.32}$% (Figure 5B), which is also due to functional groups. As seen in Figure 6, the Kubelka−Munk function may be used to assess the band gap of structures based on UV−vis DRS. The band gap (E_g) values are quite near to one other and are around 3.5 eV, which is found as the junction point of the adsorption edge in a plot of *F* versus *E*. This is because all PFDs have a high degree of structural similarity. These results showed that visible light could be used to measure the PFDs' excitable semiconductor

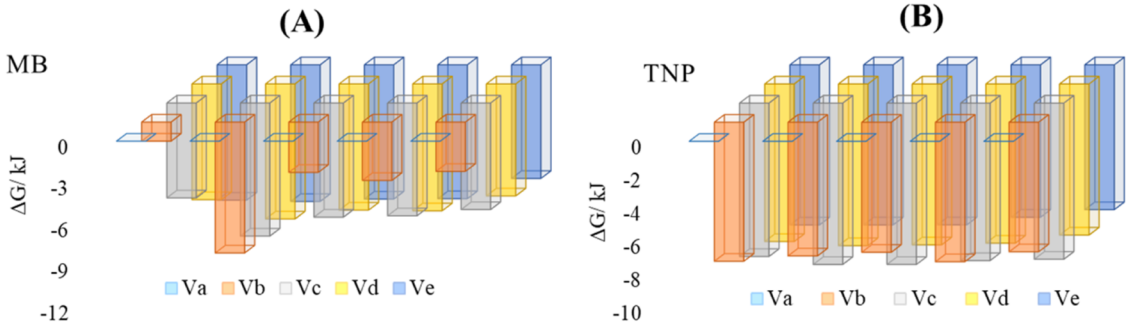

Figure 8. Comparative analysis of Gibbs function (ΔG^0) of (A) oxidation and (B) reduction of MB and TNP, respectively.

https://doi.org/10.1021/acsorginorgau.4c00063
ACS Org. Inorg. Au 2025, 5, 47−61

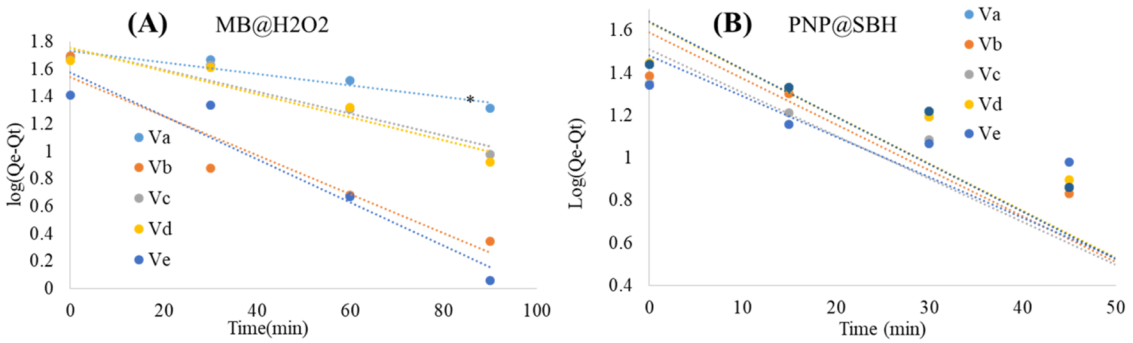

Figure 9. Pseudo-first-order kinetic study of (A) oxidation and (B) reduction of MB and TNP respectively.

Table 3. Pseudo-First-Order Kinetic Parameters for Oxidation/Reduction of MB/TNP

	TNP reduction		MB oxidation	
PFDs	K_1	R^2	K_1	R^2
Va	0.022	0.82	0.00	0.90
Vb	−0.021	0.82	−0.01	0.91
Vc	−0.020	0.81	−0.01	0.92
Vd	−0.019	0.74	−0.01	0.91
Ve	−0.022	0.82	−0.02	0.92

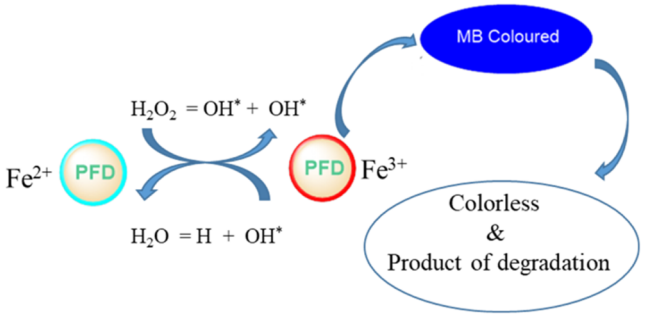

Figure 10. Oxidative degradation of dye.

status and that sunlight's visible and UV light may determine their photocatalytic activity.

3.4. DFT Investigation

A graphical representation of the HOMO and LUMO orbitals of the PFDs Va−Ve is shown in Figure 7. While the HOMO orbitals are spread across the functionality of PFDs, the LUMO orbitals are focused on the ferrocene moiety (Fe metal).[42] Generally speaking, molecules' chemical reactivity may be determined by looking at the energy levels of their HOMO/LUMO orbitals and the gaps between them. The optimized compound's most probable site for reduction is shown by the LUMO orbitals, while the HOMO orbitals indicate the preferred place for oxidation of electroactive species. When an electron is needed, the LUMO orbital functions as an electron acceptor, and when it is needed as an electron donor, it is called the HOMO orbital.[42−44] An indication of intramolecular charge transfer (ICT) interactions taking place inside a molecule is the HOMO−LUMO energy gap. The lowest unoccupied molecule orbital energy, or ELUMO, and the highest occupied molecular orbital energy, or EHOMO, enable electrons to be added and removed, respectively, when the orbital energies are lowered and oxidized. The relationship between ELUMO and EHOMO is pivotal in electron transfer processes. Lower ELUMO facilitates easier electron addition (reduction), while higher EHOMO facilitates easier electron removal (oxidation). When these energies are modified through chemical reactions like oxidation, the molecule's propensity to undergo further electron transfers can be significantly impacted. In our investigation, the ease of oxidation and reduction of MeB and TNP by PFDs followed a specific sequence: Vb > Va > Vc > Vd > Ve. This sequence correlates with the trends observed in the DFT calculations (Table 2), where the energy gap also varied accordingly.

Moreover, DFT-based calculations facilitated the determination of Mulliken charges on these molecular structures, aiding in the identification of preferred sites for reduction/oxidation processes. This analysis provided insights into the sites susceptible to electrophilic or nucleophilic attacks.[45] The graphical representation of the Mulliken charge distribution in the depicted compounds, as shown in Figure 7, reveals multiple potential sites for electrophilic and nucleophilic attacks. Electrophilic sites, characterized by their high electronegativity, are depicted in red, while nucleophilic sites, exhibiting a positive charge, are denoted in blue. Analysis of the Mulliken charge distribution facilitates predictions regarding the relative redox behavior of the compounds. For instance, the reduction potential of compound Vb suggests a more straightforward oxidation/reduction process, attributable to the presence of an indole ring acting as an electron-withdrawing group. Through DFT studies, we can effectively complement and predict the impact of various functional groups on our compounds, providing valuable insights into their reactivity and redox behavior.

3.5. Thermodynamic Parameters and Kinetics of Catalytical Activity of PFDs

To determine the maximal oxidation/reduction ability at constant temperature and pressure, the changes in Gibbs function (ΔG^0) were computed as follows[46]

$$\Delta G^\circ = -RT \ln K_D \quad \text{and} \quad K_D = \frac{q_e}{C_e}$$

Here, qe and Ce are equilibrium dye concentrations, respectively, while K_D is the thermodynamic equilibrium constant. The −ve ΔG^0 reveals the spontaneity of oxidation/reduction of MB/TNP by PFDs that increases as time increases with a constant amount of catalyst (Figure 8A,B). In terms of values, ΔG^0 is found as VbΔG^0 > VaΔG^0 > VcΔG^0 > VdΔG^0 > VeΔG^0, inferring their oxidation/reduction spontaneity. ΔG^0 data are also supported by the experimental values where Vb has shown good oxidation/reduction potential.

https://doi.org/10.1021/acsorginorgau.4c00063
ACS Org. Inorg. Au 2025, 5, 47−61

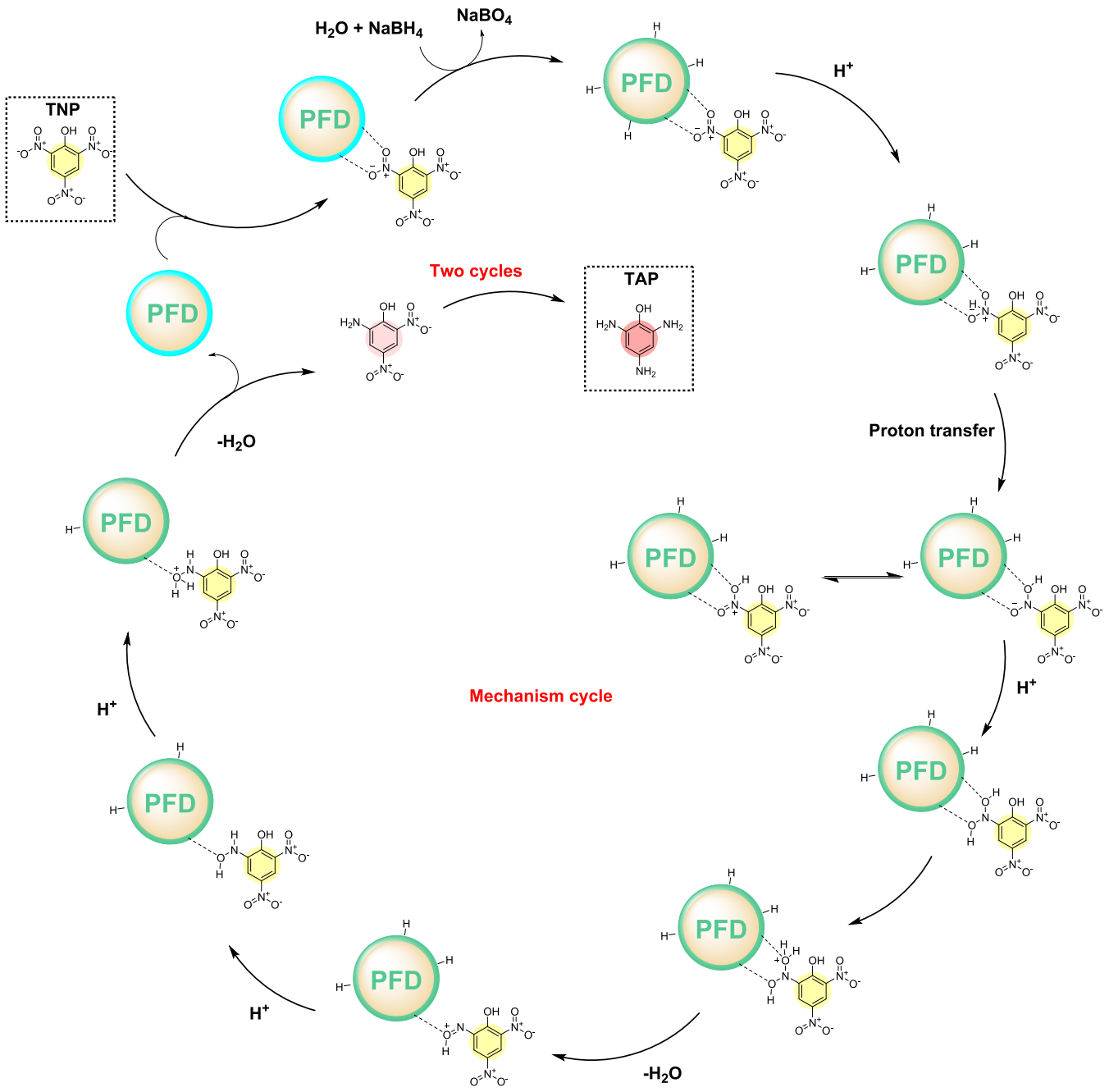

Figure 11. Reductive conversion of trinitrophenol into triaminophenol.

$$PFD + BH_4^- \longrightarrow PFD\text{-}H + PFD\text{-}BH_3^-$$
$$PFD^-H + TNP \longrightarrow TAP + PFD + H^+$$
$$PFD\text{-}BH_3^- + PNP \longrightarrow TAP + PFD + BH_3^-$$

Figure 12. Possible mechanism for the reduction reaction.

The Lagergren pseudo-first-order kinetic model is used[47,48] and provided as a means of comprehending the oxidation/reduction process with reaction pathways.

$$\frac{dq_t}{dt} = K_1(q_e - q_t)$$

After applying the boundary condition $q_t = 0$ at $t = 0$, the integrated rate law is

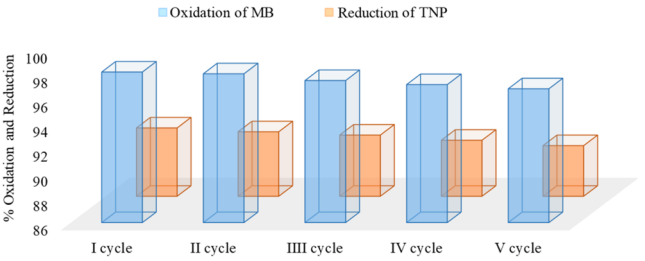

Figure 13. Recyclability of Vb as a catalyst.

$$\log(q_e - q_t) = \log q_e - \frac{K_1}{2.303}t$$

https://doi.org/10.1021/acsorginorgau.4c00063
ACS Org. Inorg. Au 2025, 5, 47−61

Table 4. Comparison of PFDs with Other Reported Materials as Redox Catalysts[49−75]

material	% degradation of MB	material	% conversion of nitrophenol
Au/Cu_2O nanospheres	90	Ir-NP film on Pd-see	75
Cu@Cu_2O nanocomposite	85	Ag-nanoplate	98
hierarchical Cu_2O	96	Au-NPs on polymer-brush	95
Cu_2O{111}-rGO	55	Ag−N	67
Ag/Cu_2O	72	hierarchical Au-sponge	40
$Cu_2O/ZnWO_4$	96	Cu Ag−Au_2 loaded protein fib	60
wheat shells	21		
activated biochar-TA	53		
MW-SiO	86		
MgAl LDO	49		
cockle shell-treated banana pith	85		
MgAl LDH	49		
alginate bead powder	48		
activated carbon	11		
Fe/SCD-LDH	83		
orange peels	18		
rice husk	40		
cotton waste	24		
Ca/Al LDH-biochar	32		
LDH-bacteria aggregates	5		
catalyst-PSFePcCFBM	99		
PFDs	99	PFDs	92

In Figure 9A,B, the straight-line graph that is derived from the plot of $\log(q_e - q_t)$ against t is used to determine the rate constant, K_1 (L/min), whereby q_t and q_e represent the quantities of oxidized/reduced MB/TNP at time t and at equilibrium. Table 3 lists the parameters for the pseudo-first-order kinetics of MB/TNP oxidation and reduction.

The oxidation/reduction of MB/TNP kinetic models of PFDs (Va-Ve) and their coefficients of determination (R^2) were both found to be close to one, indicating the validity of the data and model. The higher value of R^2 for the pseudo-first-order MB/TNP process might be explained by the fact that the rate of oxidation/reduction of this process depends on both concentration and time rather than only the concentration factor.

3.6. Proposed Mechanism for Oxidation and Reduction of PFDs

The ferrocene group's existence is what unites the two structures. Ferrocene is a transition metal compound with strong redox-reversible properties and an electron donor−acceptor conjugated structure.[33] The electron transport during the process is confirmed by the excellent reversible redox nature of ferrocene understood from CV studies.[34] Therefore, in the presence of H_2O_2, the Fc moiety may be oxidized to a cationic form (Fc^+) and then restored by an electron shift, resulting in the production of hydroxide radicals by the conversion of Fe(II) to Fe(III) (Figure 10).

One possible mechanism for the reduction reaction under study is that PFD and BH_4 separate to create PFD-H and PFD-BH_3^- (Figure 12). Because in such compounds, Fe^{2+} can accommodate H^+ and BH_3, according to the below equation. A diagrammatic way of reduction mechanism is depicted in Figure 11, where all three nitro groups of TNP are converted into amine groups as shown in Figure 12.

3.7. Catalyst Recycling

Following the catalytic experiment, Vb was retrieved and subjected to multiple washes with water. Remarkably, it retained its catalytic activity and was reused. The reusability of the same as a catalyst was examined over five cycles for both the oxidation of MB and reduction of TNP, and the results are depicted in Figure 13. Here, in each cycle, the oxidative degradation of MB was found to be about 99%, while reduction of TNP was noted to be 91%.

Table 4 represents a comparative analysis of catalytic degradation of MO and TNP where PFDs were noted as more effective for the same materials than previously studied materials.

4. CONCLUSIONS

The work explored the oxidation and reduction catalytic potential of ferrocene-based compounds against methyl blue and trinitrophenol, respectively. 99 and 92% oxidation and reduction of methyl blue and trinitrophenol have been noted with the compound Vb containing indoline substitution. Such redox potential of the compound was supported by its band gap value of 2.7 eV. The calculations for the HOMO and LUMO confirmed the stable geometry of PFDs. The negative values of HOMO and LUMO supported the oxidation and reduction performances of PFDs and varied with different substitutions. The analysis of the Lagergren pseudo-first-order kinetic model, in support of catalytic performance, revealed that the mobility of dye/phenol molecules with the PFD regulates the catalytic conversion rate.

■ ASSOCIATED CONTENT

Data Availability Statement

The data underlying this study are available in the published article and its Supporting Information.

Supporting Information

The Supporting Information is available free of charge at https://pubs.acs.org/doi/10.1021/acsorginorgau.4c00063.

NMR, LCMS, FTIR spectral data, and computational data of the synthesized compounds (PDF)

■ AUTHOR INFORMATION

Corresponding Author

Rakesh Kumar Ameta − *Department of Chemistry, Gandhinagar Institute of Science, Gandhinagar University, Gandhinagar, Gujarat 382721, India;* orcid.org/0000-0002-6018-8653; Email: ametarakesh40@gmail.com

Authors

Sagar R. Sangani − *Department of Chemistry, SMMPISR, Kadi Sarva Vishwavidyalaya, Gandhinagar, Gujarat 382023, India; Piramal Pharma Solutions, Ahmedabad, Gujarat 382213, India*

Dax Patel − *Department of Chemistry, SMMPISR, Kadi Sarva Vishwavidyalaya, Gandhinagar, Gujarat 382023, India*

https://doi.org/10.1021/acsorginorgau.4c00063
ACS Org. Inorg. Au 2025, 5, 47−61

Ranjitsinh C. Dabhi − *Department of Chemistry, University School of Sciences, Gujarat University, Ahmedabad, Gujarat 382213, India*
Tushar R. Sutariya − *Department of Chemistry, Sardar Patel University, Vallabh Vidyanagar, Gujarat 388120, India*
Sarfaraz Ahmed − *Department of Pharmacognosy, College of Pharmacy, King Saud University, Riyadh 11451, Saudi Arabia*

Complete contact information is available at: https://pubs.acs.org/10.1021/acsorginorgau.4c00063

Author Contributions

CRediT: **Sagar R. Sangani** conceptualization; **Dax Patel** conceptualization, investigation; **Ranjitsinh C. Dabhi** formal analysis; **Tushar R. Sutariya** formal analysis; **Sarfaraz Ahmed** writing - review & editing.

Notes

The authors declare no competing financial interest.

■ ACKNOWLEDGMENTS

The authors are thankful to Kadi Sarva Vishwavidhyalaya, Gandhinagar, Gujarat, for infrastructural support. The authors are also thankful to Piramal Discovery Solutions, Ahmedabad, for providing support. The authors extend their appreciation to the Researchers Supporting Project number (RSP2024R380), King Saud University, Riyadh, Saudi Arabia.

■ REFERENCES

(1) Ameta, R. K.; Singh, M. Co(III) based surfactant complexes and their Dye, BSA and free radical activities. *Heliyon* **2019**, *5* (4), No. e01568.
(2) Ameta, R. K.; Singh, M. -NO and -CN directed Metal Organic Ionic Framework used for Concentration Responsive Adsorption of Organic Pollutant, Bovine Serum Albumin and 2,2-Diphenyl-1-Picrylhydrazyl. *ChemistrySelect* **2019**, *4*, 1922−1929.
(3) Ghosh, S.; Kouamé, N. A.; Ramos, L.; Remita, S.; Dazzi, A.; Deniset-Besseau, A.; Beaunier, P.; Goubard, F.; Aubert, P. H.; Remita, H. Conducting polymer nanostructures for photocatalysis under visible light. *Nat. Mater.* **2015**, *14*, 505−511.
(4) Ameta, R. K. [Fe(CN)5NO]2−-Based MOIFs for Adsorption of Organic Pollutants and as a Self-Rotatory Motor. *ACS Omega* **2021**, *6* (1), 456−464.
(5) Xu, L.; Cheng, L.; Wang, C.; Peng, R.; Liu, Z. Conjugated polymers for photothermal therapy of cancer. *Polym. Chem.* **2014**, *5*, 1573−1580.
(6) Yang, K.; Xu, H.; Cheng, L.; Sun, C.; Wang, J.; Liu, Z. In Vitro and In Vivo Near-Infrared Photothermal Therapy of Cancer Using Polypyrrole Organic Nanoparticles. *Adv. Mater.* **2012**, *24*, 5586−5592.
(7) Chen, Q.; He, Q.; Lv, M.; Xu, Y.; Yang, H.; Liu, X.; Wei, F. Selective adsorption of cationic dyes by UiO-66-NH2. *Appl. Surf. Sci.* **2015**, *327*, 77−85.
(8) Hsu, Y. C.; Yen, C. H.; Huang, H. C. Multistage treatment of high strength dye wastewater by coagulation and ozonation. *J. Chem. Technol. Biotechnol.* **1998**, *71*, 71−76.
(9) Verma, A. K.; Dash, R. R.; Bhunia, P. Sol-Gel γ-Al2O3 Nanoparticles Assessment of the Removal of Eosin Yellow Using: Adsorption, Kinetic and Thermodynamic Parameters. *J. Environ. Manage.* **2012**, *93*, 154−168.
(10) Rouhani, F.; Rafizadeh-Masuleh, F.; Morsali, A. Selective sacrificial metal−organic frameworks: a highly quantitative colorimetric naked-eye detector for aluminum ions in aqueous solutions. *J. Mater. Chem. A* **2019**, *7*, 18634−18641.
(11) Rouhani, F.; Morsali, A. Goal-Directed Design of Metal−Organic Frameworks for HgII and PbII Adsorption from Aqueous Solutions. *Chem. - Eur. J.* **2018**, *24*, 17170−17179.
(12) Rouhani, F.; Morsali, A. Fast and Selective Heavy Metal Removal by a Novel Metal-Organic Framework Designed with In-Situ Ligand Building Block Fabrication Bearing Free Nitrogen. *Chem. - Eur. J.* **2018**, *24*, 5529−5537.
(13) Sheng, X.; Liu, Y.; Wang, Y.; Li, Y.; Wang, X.; Wang, X.; Dai, Z.; Bao, J.; Xu, X. Cesium Lead Halide Perovskite Quantum Dots as a Photoluminescence Probe for Metal Ions. *Adv. Mater.* **2017**, *29*, No. 1700150.
(14) Tovar-Gomez, R.; Rivera-Ramírez, D.; Hernandez-Montoya, V.; Bonilla-Petriciolet, A.; DuránValle, C.; Montes-Morán, M. Continuous Adsorption of Dye AB25 and Cadmium Metal in Binary Solutions on Modified Carbon. *J. Hazard. Mater.* **2012**, *199*, 290−300.
(15) Zhang, H.; Wang, X.; Liao, Q.; Xu, Z.; Li, H.; Zheng, L.; Fu, H. Embedding Perovskite Nanocrystals into a Polymer Matrix for Tunable Luminescence Probes in Cell Imaging. *Adv. Funct. Mater.* **2017**, *27*, No. 1604382.
(16) Liu, K.-G.; Rouhani, F.; Shan, Q.-D.; Wang, R.; Li, J.; Hu, M.-L.; Cheng, X.; Morsali, A. Ultrasonic-assisted fabrication of thin-film electrochemical detector of H_2O_2 based on ferrocene-functionalized silver cluster. *Ultrason. Sonochem.* **2019**, *56*, 305−312.
(17) Liochev, S. I. The Mechanism of "Fenton-Like" Reactions and Their Importance for Biological Systems: A Biologist's View. In *Metal Ions in Biological Systems*; Routledge: New York, 2018; pp 1−39.
(18) Liu, X.; Zhou, Y.; Zhang, J.; Luo, L.; Yang, Y.; Huang, H.; Peng, H.; Tang, L.; Mu, Y. Insight into electro-Fenton and photo-Fenton for the degradation of antibiotics: Mechanism study and research gaps. *Chem. Eng. J.* **2018**, *347*, 379−397.
(19) Huang, H.-H.; Lu, M.-C.; Chen, J.-N. Catalytic decomposition of hydrogen peroxide and 2-chlorophenol with iron oxides. *Water Res.* **2001**, *35*, 2291−2299.
(20) Valentine, R. L.; Wang, H. A. Iron oxide surface catalyzed oxidation of quinoline by hydrogen peroxide. *J. Environ. Eng.* **1998**, *124*, 31−38.
(21) Yeh, C. K.-J.; Chen, W.-S.; Chen, W.-Y. Production of Hydroxyl Radicals from the Decomposition of Hydrogen Peroxide Catalyzed by Various Iron Oxides at pH 7. *Pract. Period. Hazard., Toxic, Radioact. Waste Manage.* **2004**, *8*, 161−165.
(22) Cheng, M.; Ma, W.; Li, J.; Huang, Y.; Zhao, J.; Wen, Y. X.; Xu, Y. Degradation of dye pollutants by immobilized polyoxometalate with H_2O_2 under visible-light irradiation. *Environ. Sci. Technol.* **2004**, *38*, 1569−1575.
(23) Georgi, A.; Schierz, A.; Trommler, U.; Horwitz, C.; Collins, T.; Kopinke, F.-D. Humic acid modified Fenton reagent for enhancement of the working pH range. *Appl. Catal., B* **2007**, *72*, 26−36.
(24) Kumar, A.; Rana, A.; Sharma, G.; Naushad, M.; Dhiman, P.; Kumari, A.; Stadler, F. J. Recent advances in nano-Fenton catalytic degradation of emerging pharmaceutical contaminants. *J. Mol. Liq.* **2019**, *290*, No. 111177.
(25) Yang, H.; Clark, H. A. Size-Tunable DNA-Based Micelles for Deep Tumor Penetration. *Chem* **2019**, *5*, 1687−1689.
(26) Wang, Q.; Tian, S.; Ning, P. Ferrocene-Catalyzed heterogeneous fenton-like degradation of methylene blue: influence of initial solution pH. *Ind. Eng. Chem. Res.* **2014**, *53*, 6334−6340.
(27) Rouhani, F.; Rafizadeh-Masuleh, F.; Morsali, A. Highly Electroconductive Metal−Organic Framework: Tunable by Metal Ion Sorption Quantity. *J. Am. Chem. Soc.* **2019**, *141*, 11173−11182.
(28) Minero, C.; Lucchiari, M.; Vione, D.; Maurino, V. Phenol Chlorination and Photochlorination in the Presence of Chloride Ions in Homogeneous Aqueous Solution. *Environ. Sci. Technol.* **2005**, *39*, 8936−8942.
(29) He, Y.; Jiang, D. B.; Chen, J.; Jiang, D. Y.; Zhang, Y. X. Synthesis of MnO2 nanosheets on montmorillonite for oxidative degradation and adsorption of methylene blue. *J. Colloid Interface Sci.* **2018**, *510*, 207−220.

(30) Ivanets, A.; Roshchina, M.; Srivastava, V.; Prozorovich, V.; Dontsova, T.; Nahirniak, S.; Sillanpää, M.; et al. Effect of metal ions adsorption on the efficiency of methylene blue degradation onto MgFe2O4 as Fenton-like catalysts. *Colloids Surf., A* **2019**, *571*, 17−26.
(31) Adeleke, J. T.; Theivasanthi, T.; Thiruppathi, M.; Swaminathan, M.; Akomolafe, T.; Alabi, A. B. Photocatalytic degradation of methylene blue by ZnO/NiFe2O4 nanoparticles. *Appl. Surf. Sci.* **2018**, *455*, 195−200.
(32) Nguyen, C. H.; Fu, C. C.; Juang, R. S. Degradation of methylene blue and methyl orange by palladium-doped TiO2 photocatalysis for water reuse: Efficiency and degradation pathways. *J. Cleaner Prod.* **2018**, *202*, 413−427.
(33) Štěpnička, P.; Demel, J.; Čejka, J. Preparation and catalytic application of MCM-41 modified with a ferrocene carboxyphosphine and a ruthenium complex. *J. Mol. Catal. A: Chem.* **2004**, *224*, 161−169.
(34) Wang, Q.; Tian, S.; Cun, J.; Ning, P. Degradation of methylene blue using a heterogeneous Fenton process catalyzed by ferrocene. *Desalin. Water Treat.* **2013**, *51*, 5821−5830.
(35) Mehta, S. K.; Kaur, R.; Singh, S. Thermogravimetric evaluation of decomposition kinetics of metal surfactant complexes. *J. Therm. Anal. Calorim.* **2012**, *107*, 69−75.
(36) Kaur, G.; Kumar, S.; Dilbaghi, N.; Kaur, B.; Kant, R.; Guru, S.; Bhushan, S.; Jaglan, S. Evaluation of bishexadecyltrimethyl ammonium palladium tetrachloride based dual functional colloidal carrier as an antimicrobial and anticancer agent. *Dalton Trans.* **2016**, *45*, 6582−6591.
(37) Zhiltsova, E. P.; Lukashenkoa, S. S.; Ibatullinaa, M. R.; Kutyrevab, M. P.; Zakharo, L. Y. Complexation of 1-hexadecyl-4-aza-1-azoniabicyclo [2.2. 2] octane bromide with nickel nitrate in acetone. *Russ. J. Phys. Chem. A* **2016**, *90*, 1374−1378.
(38) Kaur, G.; Garg, P.; Chaudhary, G. R. Role of manganese-based surfactant towards solubilization and photophysical properties of fluorescein. *RSC Adv.* **2016**, *6*, 7066−7077.
(39) Zha, Q.; Xie, Q.; Hu, Y.; Han, J.; Ge, L.; Guo, R. Metallosurfactants Cn−Cu−Cn: vesicle formation and its drug-controlled release properties. *Colloid Polym. Sci.* **2016**, *294*, 841−849.
(40) Kaur, G.; Kumar, S.; Kant, R.; Bhanjana, G.; Dilbaghi, N.; Guru, S. K.; Bhushan, S.; Jaglan, S. One-step synthesis of silver metallosurfactant as an efficient antibacterial and anticancer material. *RSC Adv.* **2016**, *6*, 57084−57097.
(41) Patel, D.; Singh, M.; Ameta, R. K. Cr2O72−/ MnO4−based novel adsorbents: Applicable for removal of cationic and anionic organic dyes from waste water. *Inorg. Chem. Commun.* **2024**, *162*, No. 112271.
(42) Asghar, F.; Munir, S.; Fatima, S.; Murtaza, B.; Patujo, J.; Badshah, A.; Butler, I. S.; Taj, M. B.; Tahir, M. N. Ferrocene-functionalized anilines as potent anticancer and antidiabetic agents: Synthesis, spectroscopic elucidation, and DFT calculations. *J. Mol. Struct.* **2022**, *1249*, No. 131632.
(43) Lee, C.; Yang, W.; Parr, R. G. A challenge for density functionals: Self-interaction error increases for systems with a noninteger number of electrons. *Phys. Rev. B* **1998**, *37*, 785−789.
(44) Atalay, Y.; Avci, D.; BaSoglu, A. Linear and non-linear optical properties of some donor−acceptor oxadiazoles by ab initio Hartree-Fock calculations. *Struct. Chem.* **2008**, *19*, 239−246.
(45) Chandrasekar, S.; Balachandran, V.; Evans, H. S.; Latha, A. Synthesis, Synthesis, crystal structures HOMO−LUMO analysis and DFT calculation of new complexes of p-substituted dibenzyltin chlorides and 1,10-phenanthroline. *Spectrochim. Acta, Part A* **2015**, *143*, 136−146.
(46) Parmar, J.; Sangani, S. R.; Kawad, M.; Korgaokar, S.; Christy, M.; Afzal, M.; Alarifi, A.; Ameta, R. K. Imatinib cation based MOIFs with [Fe(CN)5NO]2−, [Fe(CN)6]3− [Fe(CN)6]4− as adsorbent of organic pollutants, and their protein interaction study. *J. Mol. Struct.* **2023**, *1288*, No. 135801.
(47) Duan, Y.-T.; Yao, Y.; Ameta, R. K. Removal and recovering of anionic and cationic dyes using Neem Leaf ash prepared at 250, 500 and 750 °C: Analyzed by adsorption isotherm and physicochemical parameters. *J. Mol. Liq.* **2022**, *370*, No. 121012.
(48) Sangani, S. R.; Dabhi, R. C.; Kawad, M.; Parmar, J.; Arya, P. S.; Chauhan, R. J.; Muddassir, M.; Christy, M.; Ameta, R. K. Buchwald coupling promoted benign synthesis of benzoxazine derivatives supported Cu complexes with their multipurpose potential in antimicrobial and catalytical fields. *J. Mol. Struct.* **2023**, *1285*, No. 135380.
(49) Shang, Y.; Chen, Y.; Shi, Z.-B.; Zhang, D.-F.; Guo, L. Synthesis and visible light photocatalytic activities of Au/Cu2O heterogeneous nanospheres. *Acta Phys.-Chim. Sin.* **2013**, *29* (8), 1819−1826.
(50) Xu, L.; Srinivasakannan, C.; Peng, J.; Yan, M.; Zhang, D.; Zhang, L. Synthesis of Cu-CuO nanocomposite in microreactor and its application to photocatalytic degradation. *Appl. Surf. Sci.* **2015**, *331*, 449−454.
(51) Kumar, S.; Parlett, C. M. A.; Isaacs, M. A.; Jowett, D. V.; Douthwaite, R. E.; Cockett, M. C. R.; Lee, A. F. Facile synthesis of hierarchical Cu2O nanocubes as visible light photocatalysts. *Appl. Catal., B* **2016**, *189*, 226−232.
(52) Zou, W.; Lei, Z.; Liu, L.; Wang, X.; Sun, J.; Wu, S.; Yu, D.; Tang, C.; Fei, G.; Lin, D. Multiscale Construction of Bifunctional Electrocatalysts for Long-Lifespan Rechargeable Zinc−Air Batteries. *Appl. Catal., B* **2016**, *181*, 495−503.
(53) Sun, Y.; Cai, L.; Liu, X.; Cui, Z.; Rao, P. Synergistic effect of well-defined dual sites boosting the oxygen reduction reaction. *J. Phys. Chem. Solids* **2017**, *111*, 75−81.
(54) Bulut, E.; Özacar, M.; Şengil, İ.A. Adsorption of malachite green onto bentonite: Equilibrium and kinetic studies and process design. *Microporous Mesoporous Mater.* **2008**, *115* (3), 234−246.
(55) Wang, Y.; Zhang, Y.; Li, S.; Zhong, W.; Wei, W. Enhanced methylene blue adsorption onto activated reed-derived biochar by tannic acid. *J. Mol. Liq.* **2018**, *268*, 658−666.
(56) Peres, E. C.; Slaviero, J. C.; Cunha, A. M.; Hosseini-Bandegharaei, A.; Dotto, G. L. Microwave synthesis of silica nanoparticles and its application for methylene blue adsorption. *J. Environ. Chem. Eng.* **2018**, *6*, 649−659.
(57) Qiao, Y.; Li, Q.; Chi, H.; Li, M.; Lv, Y.; Feng, S.; Zhu, R.; Li, K. Methyl blue adsorption properties and bacteriostatic activities of Mg-Al layer oxides via a facile preparation method. *Appl. Clay Sci.* **2018**, *163*, 119−128.
(58) Hasan, R.; Ying, W. J.; Cheng, C. C.; Jaafar, N. F.; Jusoh, R.; Jalil, A. A.; Setiabudi, H. D. Methylene blue adsorption onto cockle shells-treated banana pith: Optimization, isotherm, kinetic, and thermodynamic studies. *Indones. J. Chem.* **2020**, *20* (2), 368−378.
(59) Aguiar, J. E.; Bezerra, B. T. C.; Braga, B. M.; Lima, D. S.; Nogueira, R. E. F. Q.; de Lucena, S. M. P.; da Silva, I. J. Adsorption of anionic and cationic dyes from aqueous solution on non-calcined Mg-Al layered double hydroxide: Experimental and theoretical study. *Sep. Sci. Technol.* **2013**, *48* (15), 2307−2316.
(60) Purnaningtyas, M. A. K.; Sudiono, S.; Siswanta, D. Synthesis of activated carbon/chitosan/alginate beads powder as an adsorbent for methylene blue and methyl violet 2B dyes. *Indones. J. Chem.* **2020**, *20* (5), 1119−1130.
(61) Rao, V. B.; Rao, S. R. M. Adsorption studies on treatment of textile dyeing industrial effluent by fly ash. *Chem. Eng. J.* **2006**, *116* (1), 77−84.
(62) Hu, W.; Wu, X.; Jiao, F.; Yang, W.; Zhou, Y. Preparation and characterization of magnetic Fe3O4@sulfonated *β*-cyclodextrin intercalated layered double hydroxides for methylene blue removal. *Desalin. Water Treat.* **2016**, *57* (53), 25830−25841.
(63) Vadivelan, V.; Kumar, K. V. Equilibrium, kinetics, mechanism, and process design for the sorption of methylene blue onto rice husk. *J. Colloid Interface Sci.* **2005**, *286* (1), 90−100.
(64) Yavuz, E.; Bayramoğlu, G.; Arica, M. Y.; Senkal, B. F. Preparation of poly (acrylic acid) containing core-shell type resin for removal of basic dyes. *J. Chem. Technol. Biotechnol.* **2011**, *86*, 699−705.
(65) Lesbani, A.; Asri, F.; Palapa, N. R.; Taher, T.; Rachmat, A. Efficient removal of methylene blue by adsorption using composite

https://doi.org/10.1021/acsorginorgau.4c00063
ACS Org. Inorg. Au 2025, 5, 47−61

based Ca/Al layered double hydroxide-biochar. *Global NEST J.* **2020**, *22*, 250−257.
(66) Liu, J.; Li, X.; Luo, J.; Duan, C.; Hu, H.; Qian, G. Enhanced decolourisation of methylene blue by LDH-bacteria aggregates with bioregeneration. *Chem. Eng. J.* **2014**, *242*, 187−194.
(67) Scheuerlein, M. C.; Muench, F.; Kunz, U.; Hellmann, T.; Hofmann, J. P.; Ensinger, W. Electroless Nanoplating of Iridium: Template-Assisted Nanotube Deposition for the Continuous Flow Reduction of 4-Nitrophenol. *ChemElectroChem* **2020**, *7*, 3496−3507.
(68) Muench, F.; Popovitz-Biro, R.; Bendikov, T.; Feldman, Y.; Hecker, B.; Oezaslan, M.; Rubinstein, I.; Vaskevich, A. Nucleation-Controlled Solution Deposition of Silver Nanoplate Architectures for Facile Derivatization and Catalytic Applications. *Adv. Mater.* **2018**, *30*, No. 1805179.
(69) Song, L.; Le, Z.; Bing, Li.; Huacheng, Z. Fullerene-containing pillar[n]arene hybrid composites. *Org. Biomol. Chem.* **2022**, *20*, 8176−8186.
(70) Muench, F.; Rauber, M.; Stegmann, C.; Lauterbach, S.; Kunz, U.; Kleebe, H. J.; Ensinger, W. Ligand-optimized electroless synthesis of silver nanotubes and their activity in the reduction of 4-nitrophenol. *Nanotechnology* **2011**, *22*, No. 415602.
(71) Yu, Y.; Xiao, W.; Zhou, T.; Zhang, P.; Yan, C.; Zheng, Z. Monolithic hierarchical gold sponges for efficient and stable catalysis in a continuous-flow microreactor. *Mater. Chem. Front.* **2017**, *1*, 482−486.
(72) Khalil, A. M.; Georgiadou, V.; Guerrouache, M.; Mahouche-Chergui, S.; Dendrinou-Samara, C.; Chehimi, M. M.; Carbonnier, B. Antimicrobial behavior and photostability of polyvinyl chloride/1-vinylimidazole nanocomposites loaded with silver or copper nanoparticles. *Polymer* **2015**, *77*, 218−226.
(73) Khajone, V. B.; Balinge, K. R.; Patle, D. S.; Bhagat, P. R. Synthesis and characterization of polymer supported Fe-phthalocyanine entangled with carboxyl functionalized benzimidazolium moiety: a heterogeneous catalyst for efficient visible-light-driven degradation of organic dyes from aqueous solutions. *J. Mol. Liq.* **2019**, *288*, No. 111032.
(74) Raut, S. U.; Balinge, K. R.; Deshmukh, S. A.; Barange, S. H.; Mataghare, B. C.; Bhagat, P. R. Solvent/metal-free benzimidazolium-based carboxyl-functionalized por-phyrin photocatalysts for the room-temperature alkyla-tion of amines under the irradiation of visible light. *Catal. Sci. Technol.* **2022**, *12* (19), 5917−5931.
(75) Mataghare, B. C.; Bhagat, P. R. Construction of porphyrin-based photocatalyst comprising pyridinium ionic liquid moiety for the metal-free visible light-assisted N-arylation of amines: facile approach to afford drug in-termediates. *New J. Chem.* **2023**, *47* (47), 21764−21780.

https://doi.org/10.1021/acsorginorgau.4c00063
ACS Org. Inorg. Au 2025, 5, 47−61